Magnetic Induction Machines Integrated Into Bulk-Micromachined Silicon

David P. Arnold, *Member, IEEE*, Sauparna Das, *Member, IEEE*, Florent Cros, Iulica Zana, *Member, IEEE*, Mark G. Allen, *Senior Member, IEEE*, and Jeffrey H. Lang, *Fellow, IEEE*

Abstract—This paper presents the design, fabrication, and characterization of laminated, magnetic induction machines intended for high-speed, high-temperature, high-power-density, silicon-based microengine power generation systems. Innovative fabrication techniques were used to embed electroplated materials (Cu, $Ni_{80}Fe_{20}$, $Co_{65}Fe_{18}Ni_{17}$) within bulk-micromachined and fusion-bonded silicon to form the machine structures. The induction machines were characterized in motoring mode using tethered rotors, and exhibited a maximum measured torque of 2.5 μN·m.   [1466]

Index Terms—AC generators, induction machines, magnetic materials, MEMS, micromachining.

I. INTRODUCTION

THE power demands of modern electronic devices are quickly outpacing the energy and power density of today's best batteries. This has driven the development of compact, electric power sources in the 10–100 W range for use in portable electronics, remotely located sensors, and robotic devices. One potential system is a gas-turbine microengine [1], [2] comprising a small (few cubic centimeters) gas-fueled turbine engine for converting fuel energy to mechanical energy and an electrical power generator for converting mechanical power into usable electrical power. Such a system has the potential to reduce the mass, life-cycle costs, and cumbersome logistics of conventional batteries while providing uninterrupted high density power.

Silicon-based, micromachined turbomachinery has been under investigation since the mid–1990s [1]–[4]. Relevant progress has been made using bulk-micromachining and wafer-bonding of multiple silicon wafers to form suitable structures [3], and both microscale combustion [3] and ultra high-speed rotation have been independently achieved [4]. Microscale electrical machines (motors and generators) have also been investigated since the early 1990's. Both variable-reluctance [5]–[7] and permanent-magnet machines [8]–[15] have been demonstrated. Typically, these machines operated at speeds less than 200 krpm and could deliver up to 100 μN·m of torque as motors or electrical output power in the mW range as generators. However, none meet the design requirements for use in a high-speed, high-power-density microturbine engine system.

To achieve the desired power densities, and for compatibility within a microturbine engine, the electrical generator must support high rotor spin speeds ($\sim$1 Mrpm). Furthermore, it must withstand high operating temperatures ($\sim$300 °C) in close proximity to the fuel-burning engine. Also, for monolithic integration within a multi-wafer-bonded microengine, the machine must be constructed using compatible fabrication processes. To achieve these goals, both electric-[15], [16] and magnetic-[17]–[19] induction machines have been targeted for use in silicon-based microturbine engines, primarily because these types of machines use simple, axisymmetric rotor structures.

As compared to their electric counterparts, magnetic machines may offer higher power densities, higher efficiencies (e.g., lower windage losses), less stringent fabrication tolerances (e.g., larger air gap), and simpler power electronics. They also operate at lower voltages and higher currents and are therefore easier to integrate with typical electronic devices. Previously investigated magnetic induction machines were fabricated using SU-8 micromolding and multi-level electroplating of various metals [18]. These first-generation devices successfully demonstrated electromechanical power conversion, but were not integrable with the silicon-based microturbines and were limited in temperature due to the presence of the SU-8 polymer [17]–[19]. This paper presents a new approach to achieve silicon-based, wafer-bonded, high-temperature, laminated, magnetic induction machines [20]. The results presented here represent a technological advancement toward fully integrated electrical power generators for silicon-based microengines.
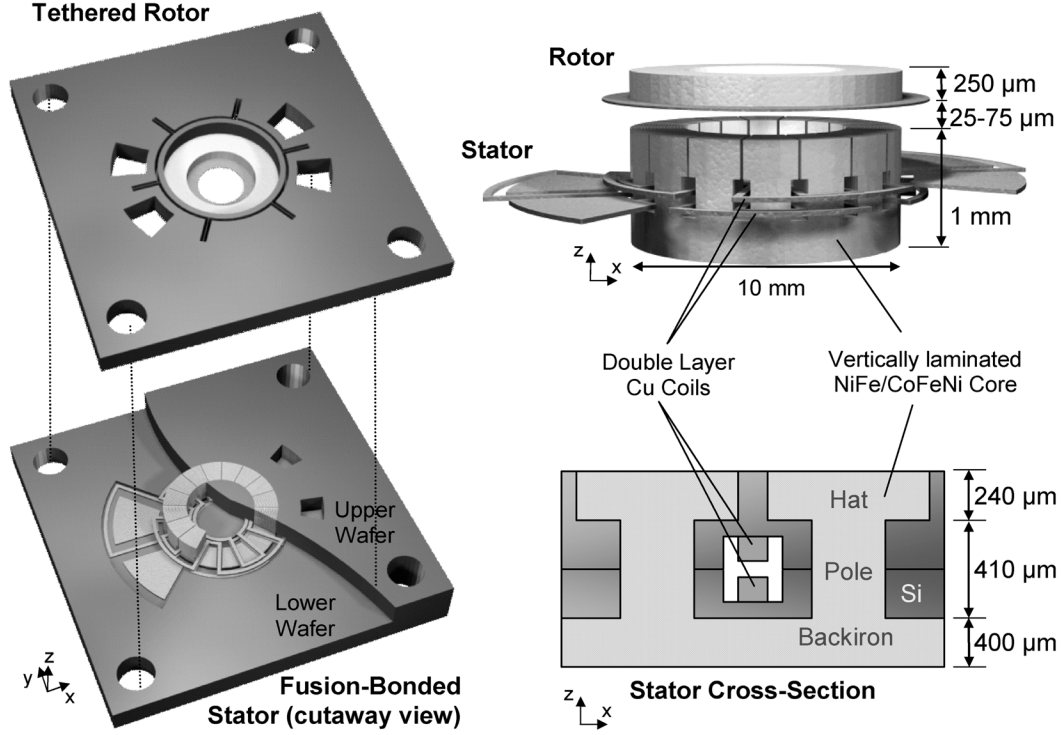
Fig. 1. Renderings of the magnetic induction machine (not drawn to scale).

II. INDUCTION MACHINE DESIGN

The magnetic machine is designed for maximum power density and efficiency in the context of interoperability with a microturbine system. As a result, the design is constrained by system level compatibility issues and microfabrication limitations. First, the turbine-generator system is intended to operate with a ∼10-mm OD rotor spinning with a 500 m/s tip speed (∼1 Mrpm rotation speed). Second, to support the high currents and magnetic fluxes needed for high power density, the machine must have relatively large geometric dimensions (∼mm). Finally, as mentioned previously, the machine should withstand operating temperatures of ∼300 °C and be fabricated using silicon wafer-bond compatible processes.

Within these constraints, a planar induction machine was designed consisting of two primary components: a two-phase, 8-pole stator and a composite annular rotor, as shown in Fig. 1. Electromechanical energy conversion occurs through the interaction of a traveling magnetic wave in the rotor-stator air gap and the eddy currents induced in the rotor by the traveling wave [21]. In motoring mode, a traveling magnetic wave is established by applying two currents in quadrature to the two stator phases, which results in a net torque and pull-in force acting on the rotor.

The stator contains two phases made up of planar Cu coils in two separate metal layers. The phases are wound with two slots per pole and one turn per slot in a three-dimensional (3-D), vertically laminated ferromagnetic core, all supported by a silicon frame. The core laminations form onion-like concentric rings,

where the lamination thickness is approximately one skin depth ($\delta \approx 30$ μm at 1 Mrpm) to limit eddy current losses [22]. The rotor is a 250-μm thick ferromagnetic annular ring (10-mm OD, 6-mm ID) with a 20-μm thick overlayer of Cu. The Cu extends beyond the magnetic region (12-mm OD, 4-mm ID) to enhance eddy current generation in the rotor for maximum torque. Additional modeling of the induction machines is reported in [23].

Machines were designed using either $Ni_{80}Fe_{20}$ or $Co_{65}Fe_{18}Ni_{17}$ as the ferromagnetic material. As compared to NiFe, the CoFeNi alloy has similar permeability and resistivity, but offers higher saturation flux density (higher power density) and higher Curie temperature (higher operating temperature) at the expense of a slight increase in coercivity (larger hysteresis loss) [24].

For testing purposes, the rotor was suspended above the stator using flexible silicon tethers that permitted angular rotation and a controllable air gap while avoiding the difficulties of supporting a fully spinning rotor. This also eliminates any uncertainty in bearing losses during torque measurements. The use of tethered rotors simulates a blocked-rotor test (slip frequency equals the electrical frequency and no mechanical losses), commonly used to test macroscale machines [21]. Six, 35-μm wide, 475- μm tall, 2.5-mm long silicon tethers were designed to provide an angular compliance of 25 rad/N·m with an axial compliance of 4.2 μm/N to prevent rotor pull-in. During testing, small angular deflections could be detected by monitoring the movement at the outer radius (5.5 mm) of the silicon ring. For small angles, this movement was approximated as a linear displacement and corresponded to a predicted deflection of 0.14 μm per μN·m of torque.
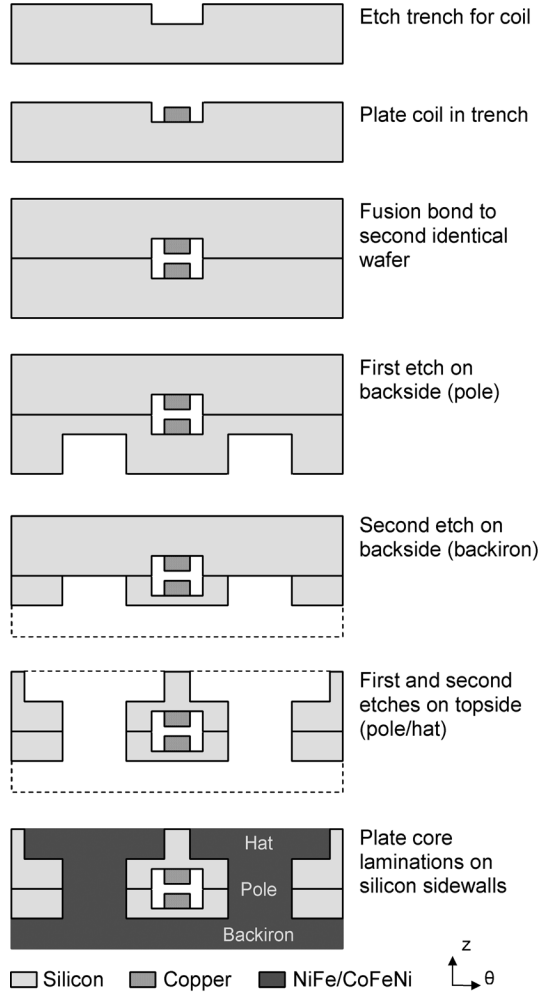
Fig. 2. Simplified fabrication process flow for wafer-bonded machine stator, depicting cross sections in θ-z plane: two coil conductors pass radially through the laminated core structure (laminations not shown).

III. DEVICE FABRICATION

Innovative fabrication techniques were used to embed thick electroplated coils and cores within etched and wafer-bonded silicon to form the machine stators. The rotors and silicon tether structures were fabricated separately and assembled together for rapid prototyping with the stators.

A. Stator Fabrication

Stators were fabricated by embedding coils inside of fusion-bonded silicon wafers and then building the magnetic core around the coils as depicted by Fig. 2. The process began with two low-resistivity (~ 0.001 Ω·cm), n-type, 100-mm diameter, double-side-polished, silicon wafers. In each wafer, 70-μm deep cavities were etched using deep reactive ion etching (DRIE), and a 200 nm thermal SiO_2 layer was grown. Then, a 400-nm Ta diffusion barrier and 200-nm Cu seed layer were DC sputtered across the surfaces of the wafers. Next, a thick negative photoresist was patterned in the cavities to define a mold for the coils, maintaining a minimum clearance of 50 μm from the cavity sidewalls. Patterning the mold within

the cavities permitted uniform plating and prevented protrusions, which would inhibit wafer bonding. After plating, the photoresist, metallic seed layers, and SiO_2 were wet-etched back down to the pristine silicon surface, leaving the coil recessed in the cavity, as shown in Fig. 3. The two wafers were then aligned and fusion bonded, sealing the coils inside. The bonding was performed at 500 °C for four hours under vacuum ($<2 \times 10^{-6}$ torr) with 200-kPa clamping pressure, resulting in a strong, uniform bond without degrading the embedded copper, as reported in [25].

At this point, processing began anew to form the stator core. First, a 3-μm PECVD oxide was deposited on the top and bottom surfaces of the bonded pair. Using this oxide layer and photoresist as masks, nested deep silicon etches were performed from the bottom and top sides to form a silicon skeleton for the laminated core. Then, using a method detailed in [26], $\sim$30 μm of NiFe or CoFeNi was selectively electroplated onto the conductive silicon sidewalls to form the magnetic laminations. The metals plated only on the etched silicon regions, with the SiO_2 layer on the top and bottom surfaces acting as a mask. Finally, contact openings were made from the top side by etching the silicon down to the buried coil contacts. Fig. 4 shows images of the completed stator, with corresponding cross sections shown in Fig. 5.

B. Tethered Rotor Fabrication

For rapid prototyping, the metallic rotors and silicon tether structures were fabricated separately and hand assembled. Rotors were built on a silicon substrate by first electroplating a 250-μm thick NiFe or CoFeNi annular ring on top of a 20-μm thick Cu ring using SU-8 molds, as shown in Fig. 6. The SU-8 was then mechanically removed, and the silicon substrate was etched away using KOH. An electroplated rotor, still attached to the silicon substrate, is shown in Fig. 7. The silicon tether structures were formed separately by through-etching a wafer using DRIE, as shown in Fig. 8. The rotors were subsequently glued into the tethered retaining ring.

IV. CHARACTERIZATION

After fabrication, the induction machines were characterized in three stages: (A) electrical measurements of the stators, (B) ferrofluid tests of the stator, and (C) tethered rotor torque measurements.

A. Stator Electrical Characterization

The induction machine stators were initially characterized using electrical measurements. Four point resistance measurements of the coils indicated an average coil resistance of 0.20 Ω. With a cross section of $A = 35$ μm $\times$ 300 μm, a total length of $L = 110$ mm, and an ideal resistivity of $\rho = 1.7$ $\mu\Omega$·cm, the predicted resistance was 0.18 Ω. Considering some variability in the conductivity and dimensions of the plated coils and that current crowding effects in the serpentine winding were not considered, the measurements agree reasonably well with the predicted values.
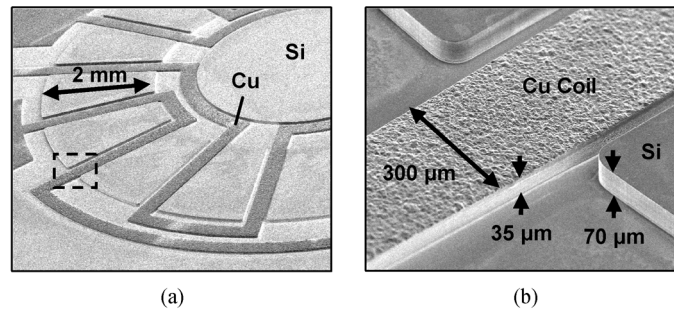
(a)   (b)

Fig. 3.   (a) SEM of 35-μm thick, 300-μm wide, copper coil recessed in 70-μm deep silicon cavity before wafer bonding to a second identical wafer; (b) detail SEM.
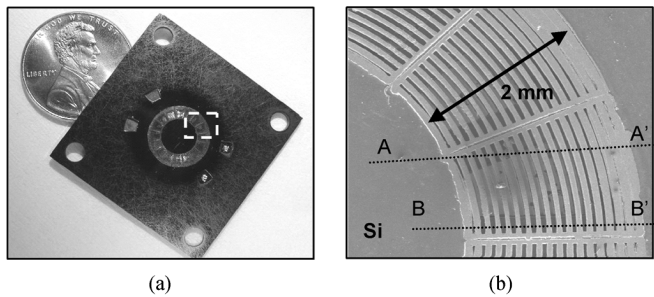

(a)   (b)

Fig. 4.   (a) Fabricated wafer-bonded machine stator. (b) Detail SEM showing NiFe vertical magnetic laminations.
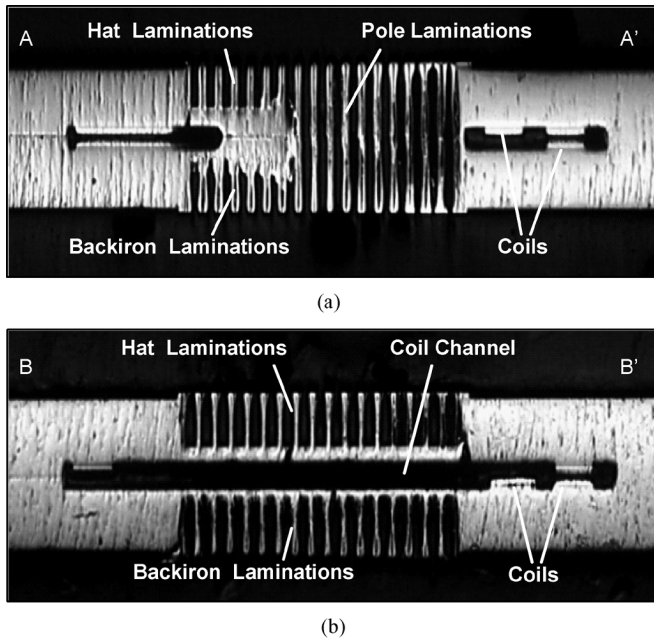

(a)

(b)

Fig. 5.   Cross sections along (a) A-A' and (b) B-B' for induction machine stators, as shown in Fig. 4(b).

Fig. 6.   Process flow for induction machine rotors.
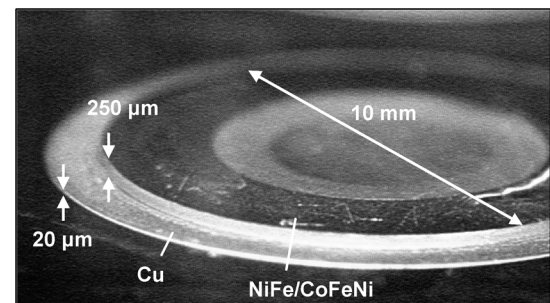
Fig. 7.   Photograph of electroplated induction machine rotor on Si substrate before release.

Inductance measurements were also made from 1 kHz – 1 MHz using an HP4194 impedance analyzer. Fig. 9 shows the frequency-dependence of each coil for both the NiFe and CoFeNi machines. The solid curves indicate the inductance of the stator alone, while the dashed curves indicate the inductance of the stator when the rotor was placed on the stator using a 25-μm thick Kapton spacer to simulate an operational air gap. Note that these measurements were conducted at low voltage/current, and would not capture saturation effects.
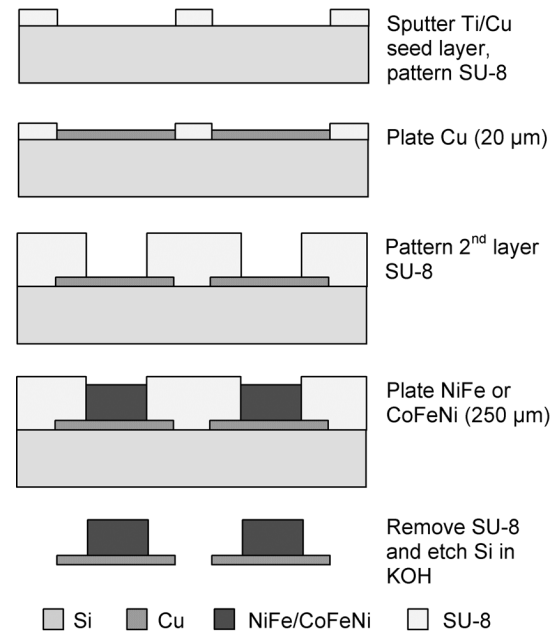
The inductance of the stator alone is seen to be fairly constant until ∼100 kHz, upon which eddy currents induce a roll off. This flat band and subsequent roll off indicated that the lamination scheme was working as expected. The roll off frequency corresponds to a synchronous mechanical speed of 1.5 Mrpm, well above the design speed. The addition of the rotor results in an increase in the low-frequency inductance, caused by an overall decrease in the total reluctance (reduced flux path length

Fig. 8.   (a) Photograph and (b) detail SEM of silicon tether structures.

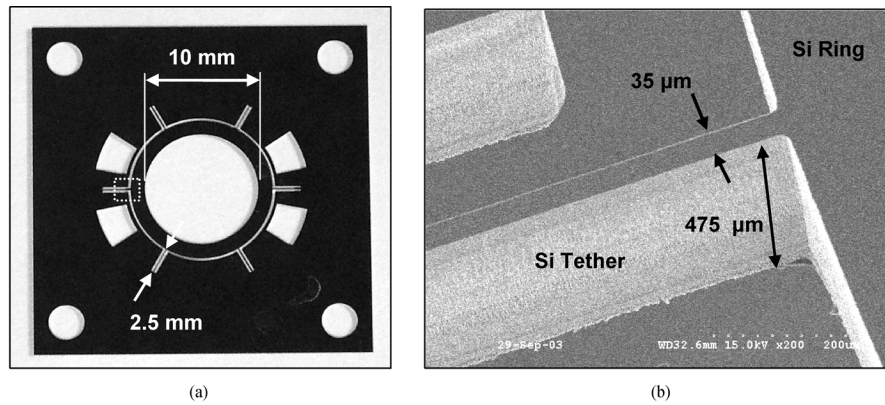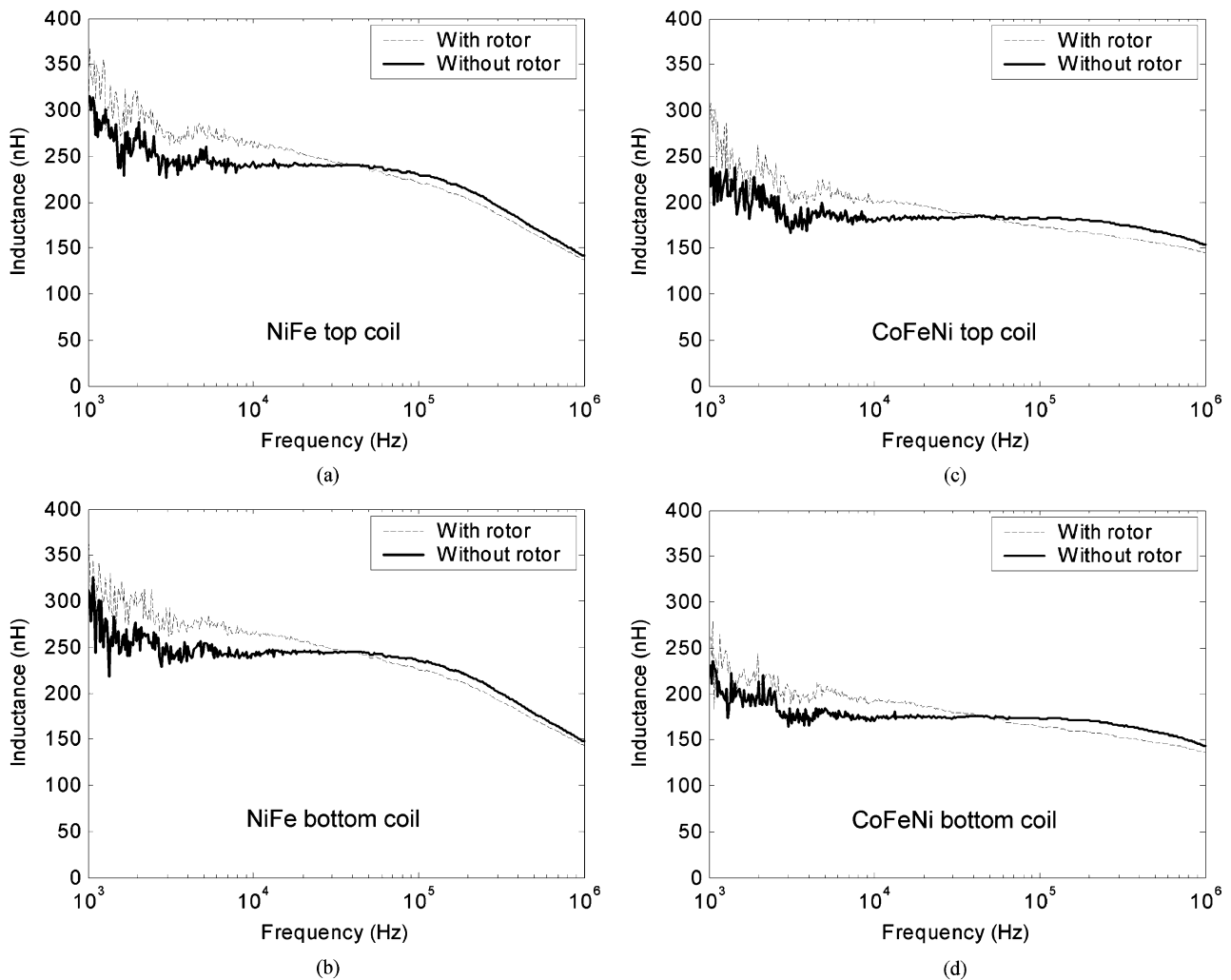Fig. 9.   Inductance of stator coils with and without rotor. (a) and (b) are the NiFe top and bottom coils, respectively, and (c) and (d) are the CoFeNi top and bottom coils, respectively.

through the air). Here, the eddy current roll off occurs earlier because the rotor is not laminated. Good agreement is also noted between the upper and lower coils for each machine.

B. Ferrofluid Tests

A ferrofluid, a colloidal suspension of magnetic particles in a liquid (oil) carrier, was used to further verify proper operation

of the stator. A small tub was constructed from a 500-μm thick ring of silicon glued to a 500-μm thick Kapton film and placed over the stator, as shown in Fig. 10. The tub was filled with a thin layer of ferrofluid (Ferrotec Corporation, Nashua, NH) that interacts with the magnetic fields produced by the stator. By exciting the stator coils at low frequency (1.5 Hz), both standing and traveling magnetic waves could be seen by the naked eye.
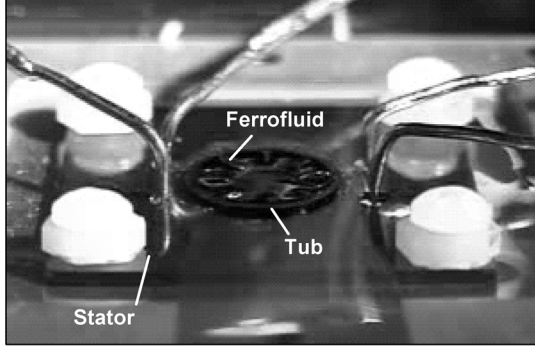
Fig. 10. Video image frame grab of traveling magnetic wave on the surface of the stator, as indicated by the peaks and valleys in the ferrofluid.
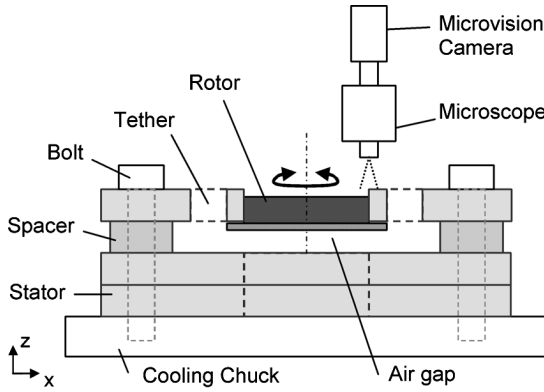

Fig. 11. Schematic of the measurement setup showing the tethered rotor structure clamped to the stator on the cooling chuck with the air gap set by Kapton spacers.

Standing waves were achieved by applying currents in-phase or 180° out of phase. Traveling waves were achieved by applying currents at ±90°. This technique enabled direct verification of the full functionality of the stator.

C. Tethered Rotor Torque Measurements

For torque measurements, the rotor was suspended above the stator with flexible silicon tethers. The stator and tethered rotor components were clamped together and mounted on a water-cooled chuck, as shown in Fig. 11. Air gaps of 25–75 μm were maintained between the stator and rotor by using Kapton spacers.

Power electronics supplied a balanced current excitation in quadrature to the stator phases creating a motoring torque. The drive signals were routed through a circuit that could swap the phases to control the direction of the traveling magnetic wave and resulting torque. This circuit was used to cyclically alternate the torque direction and excite the tethered rotor into mechanical oscillation at a specific frequency (the *torque reversal* frequency). Note, the torque reversal frequency (<1 kHz) was much lower than the electrical coil frequency (tens of kHz). The system dynamics are governed by a second-order system response $T = J\ddot{\theta} + b\dot{\theta} + k\theta$, where T is the torque, θ is the angular displacement, J is the moment of inertia, b is the damping factor, and k is the net angular spring coefficient.

A microvision image analysis system was used to dynamically measure the displacement of the outermost radius of the rotor silicon ring under the influence of the oscillating torque input, as described in [18]. This method offered two primary benefits over using static measurements. First, larger deflections could be obtained near the mechanical resonant frequency, which were easier to measure. Second, the spring stiffness could be extracted from the measurements, rather than estimated from the geometry of the tethers. This was important considering the dimensions of the microfabricated tethers were prone to large uncertainties.

In practice, the torque reversal frequency was incrementally stepped from 10 Hz to 1 kHz, while monitoring the resulting angular deflection. This procedure was controlled entirely by the microvision image analysis system. A typical frequency response of the angular displacement is shown in Fig. 12 and is seen to closely follow a standard second-order system response. For each such curve, the torque was extracted by fitting a second-order response to the measured data. The linear resolution of the image analysis system was ∼4 nm, corresponding to an angular resolution of 7.3×10^{-7} rad and a torque resolution of 30 nN·m.

Machines were analyzed in motoring mode by varying both the amplitude (2–8 A_{pk}) and frequency (2.5–55 kHz) of the excitation currents and also the air gap (25–75 μm). The machines show characteristic induction machine behavior, as shown in Figs. 13 and 14. These plots represent torque-slip curves, as the machines were tested under blocked-rotor conditions [21]. The error bars indicate 95% confidence intervals, based on the accuracy of the curve fit to the dynamic response data. The tethered motor testing was limited to a maximum of 8 A_{pk} (approximately 6.4 W per phase, for 0.2-Ω coil resistance) because the displacement of the rotor became nonlinear and out-of-plane motion was detected, both causing large uncertainties in the torque extraction. The NiFe machine shows a maximum torque of 2.5 μN·m at 8 A_{pk}, 35 kHz. Tests of the CoFeNi machine were corrupted at high currents by broken tethers, and no valid data was collected above 6 A_{pk}. Regardless, the CoFeNi machine demonstrated 1.0 μN·m at 6 A_{pk}, 25 kHz.

At low currents, where no magnetic saturation occurs, the torque should show a quadratic dependence with current; upon saturation, the torque should increase linearly. Fig. 15 plots the torque versus the *square* of current. The data follows this quadratic relation, indicating that neither machine had saturated, and that higher currents may be used to achieve even larger torques. While not measured, the machine should support currents of at least 32 A_{pk} (corresponding to a current density of 3×10^9 A/m^2). However, the machine modeling [23] indicated that the onset of saturation should occur around 6 A_{pk} and >8 A_{pk} for the NiFe and CoFeNi machines, respectively. Thus, any further increase in current would theoretically result in a proportional (rather than quadratic) increase in torque. This transition to saturation cannot be clearly determined from the experimental data shown in Fig. 15 because of the small number of data points.
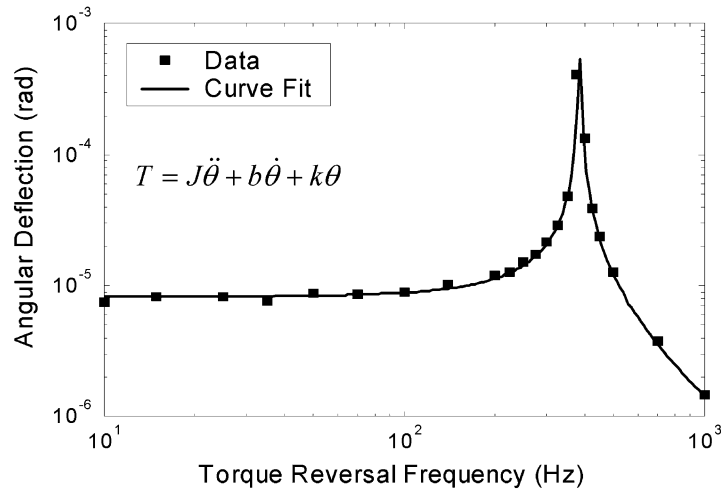
Fig. 12.   Example dynamic response of the oscillating tethered rotor as a function of the torque reversal frequency, showing measured data and a second-order curve fit used to extract torque, T, from the deflection, θ.
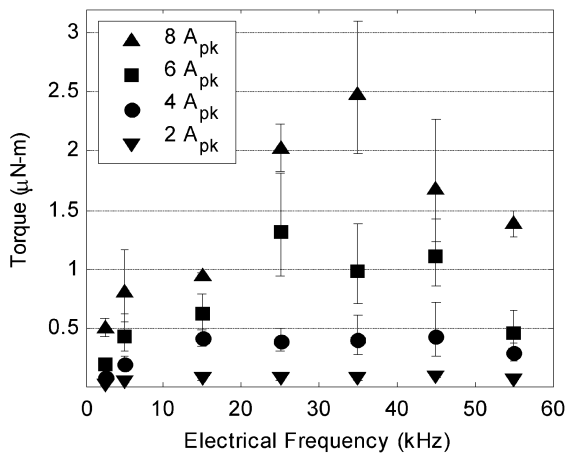

Fig. 13.   NiFe machine measured torque-slip curves—torque versus electrical (slip) frequency—for currents of 2–8 A_{pk} with 50 μm air gap.
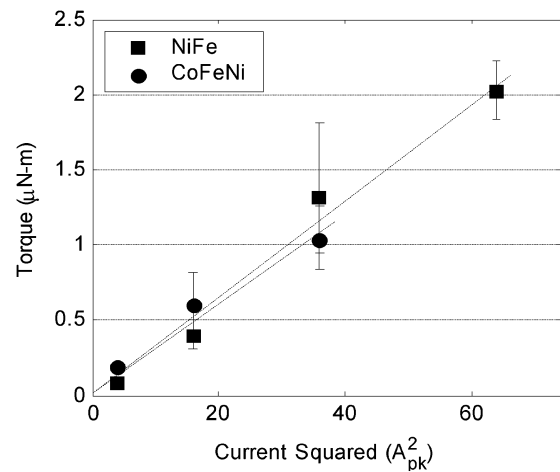
Fig. 15.   Torque versus square of stator current for NiFe and CoFeNi machines at 25 kHz with 50 μm air gap.
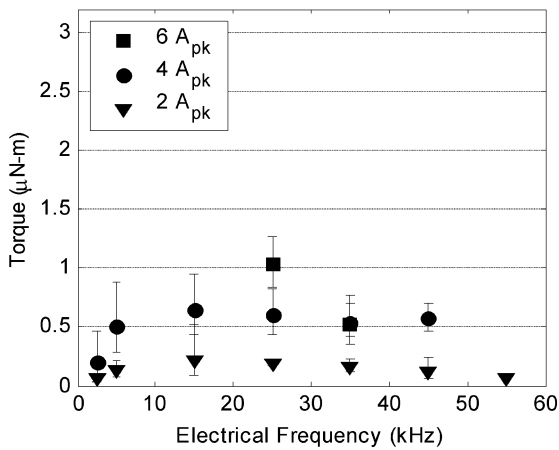
Fig. 14.   CoFeNi machine measured torque-slip curves—torque versus electrical (slip) frequency—for currents of 2–6 A_{pk} with 50 μm air gap.
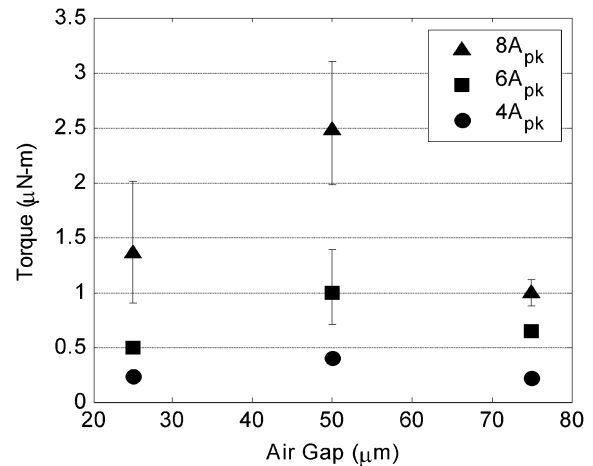
Fig. 16.   Torque versus air gap for NiFe machine for 4, 6, and 8 A_{pk} at 35 kHz.

Fig. 16 shows the torque for the NiFe machine as a function of the air gap for three different current amplitudes at 35 kHz. Torque is seen to be maximized for the 50 μm air gap, and is explainable as follows. As the air gap is increased, the inductive coupling between the stator and rotor is reduced, and the magnitude of the rotor eddy currents and the resulting torque are also reduced. However, as the air gap is reduced, higher-order spatial harmonics from the traveling magnetic wave couple into the stator. These harmonics rotate in opposition to the mechanical

rotation and act as braking harmonics that reduce the net torque [27]. These two opposing effects result in an optimum air gap.

V. CONCLUSION

The successful development of laminated, fusion-bonded, Si-based, magnetic machines represents progress toward a fully integrated microengine system. The materials, structure, and fabrication processes offer the potential for higher operating temperatures and direct integration with multiwafer microturbine devices.

The maximum demonstrated torque of 2.5 μN · m for these silicon-based machines is higher than the previously reported SU-8-based magnetic induction machine [17]–[19]. However, some of this improvement is attributed to the larger machine size. With an active volume of 75 mm^3 (10 mm ID, 6 mm OD, 1.5 mm thick), the NiFe machines have a torque density of 33 N·m/m^3 and an average surface shear stress of 12 N/m^2 acting on the rotor surface. The average surface shear stress normalizes the torque by the rotor surface area and moment arm and represents the average force per unit area generated in the rotor by the electromechanical interactions.

Although the machines were tested in a blocked-rotor condition, the torque-slip curves can provide insight into operation under fully spinning conditions. To first order, the torque-slip curves should remain constant with rotor mechanical frequency [21]. Thus, output mechanical power can be estimated by multiplying the measured torque by the mechanical frequency, ω_m, where $\omega_m \approx 10^5$ rad/s for the design speed of 1 Mrpm. Therefore, the 2.5 μN·m peak torque corresponds to a peak motoring power of 0.25 W at design speed. Ignoring all other loss mechanisms (magnetic core loss, mechanical friction, windage, etc.) the total losses are estimated by the two-phase I^{2}R conduction losses in the windings. Under peak power conditions, the input current was 8 A$_{pk}$, which corresponds to 12.8 W of input power and an efficiency of 1.9%. These results provide some measure of the machine motoring performance, but to effectively demonstrate generation would require a spinning rotor.

Finally, the performances of the machines reported here are limited by two fabrication issues. First, the teeth gaps between adjacent poles on the upper surface of the stator core are partially closed over due to overplating of the laminations. This partially shorts out the magnetic flux path between the stator and rotor and limits torque production. Second, in using highly doped silicon for the stator frame, the eddy currents, which would normally be confined to small loops around each lamination, are allowed to circulate through the stator frame around an entire stator pole. These large eddy current loops reduce the flux linking the stator and rotor and limit the effectiveness of the laminations. Rebuilding machines with a nonconductive stator frame, larger coils, and more aggressive fabrication could also further improve the performance.

REFERENCES

[1] A. H. Epstein *et al.*, "Power MEMS and microengines," in *Proc. Tech. Dig. Int. Conf. Solid-State Sensors Actuators, (Transducers'97)*, Jun. 1997, pp. 753–756.

[2] A. H. Epstein and S. D. Senturia, "Macro power from micro machinery," *Science*, vol. 276, no. 5316, p. 1211, May 1997.

[3] A. Mehra *et al.*, "A six-wafer combustion system for a silicon micro gas turbine engine," *J. Microelectromech. Syst.*, vol. 9, pp. 517–27, 2000.

[4] L. G. Frechette *et al.*, "Demonstration of a microfabricated high-speed turbine supported on gas bearings," *Proc. Tech. Dig. Solid-State Sensor Actuator Workshop (Hilton Head 2000)*, pp. 43–7, Jun. 2000.

[5] H. Guckel *et al.*, "A first functional current excited planar rotational magnetic micromotor;," in *Proc. IEEE Micro Electro Mechanical Systems (MEMS'93)*, Feb. 1993, pp. 7–11.

[6] ——, "Planar rotational magnetic micromotors," *Int. J. Appl. Electromagn. in Mat.*, vol. 4, no. 4, pp. 377–382, June 1994.

[7] C. H. Ahn, Y. J. Kim, and M. G. Allen, "A planar variable reluctance magnetic micromotor with fully integrated stator and coils," *J. Microelectromech. Syst.*, vol. 2, no. 4, pp. 165–73, Dec. 1993.

[8] B. Wagner, M. Kreutzer, and W. Benecke, "Permanent magnet micromotors on silicon substrates," *J. Microelectromech. Syst.*, vol. 2, no. 1, pp. 23–29, Mar. 1993.

[9] K.-P. Kamper *et al.*, "Electromagnetic permanent magnet micromotor with integrated micro gear box," in *Proc. 5th Int. Conf. New Actuators, (Actuator'96)*, June 1996, pp. 429–432.

[10] S. Kleen, W. Ehrfeld, F. Michel, and H.-D. Stölting, "Penny-motor: A family of novel ultraflat electromagnetic micromotors," in *Proc. 8th Int. Conf. New Actuators (Actuator 2000)*, June 2000, pp. 193–196.

[11] P.-A. Gilles, J. Delamare, O. Cugat, and J.-L. Schanen, "Design of a permanent magnet planar synchronous micromotor," in *Proc. 35th Mtg. IEEE Ind. Appl. Soc.*, vol. 1, Oct. 2000, pp. 223–227.

[12] C. Yang *et al.*, "An axial flux electromagnetic micromotor," *J. Micromech. Microeng.*, vol. 11, pp. 113–117, 2001.

[13] H. Raisigel *et al.*, "Magnetic planar micro-generator," in *Proc. 18th Int. Workshop on High Performance Magnets and their Applications*, Annecy, France, Aug.–Sep. 29–2, 2004.

[14] A. S. Holmes, G. Hong, and K. R. Buffard, "Axial-flux permanent magnet machines for micropower generation," *J. Microelectromech. Syst.*, vol. 14, no. 1, pp. 54–62, Feb. 2005.

[15] L. G. Frechette *et al.*, "An electrostatic induction micromotor supported on gas-lubricated bearings," in *Proc. Tech. Dig. 14th IEEE Int. Conf. MEMS (MEMS 2001)*, Jan. 2001, pp. 290–293.

[16] C. Livermore *et al.*, "A high-power MEMS electric induction motor," *J. Microelectromech. Syst.*, vol. 13, no. 3, pp. 465–471, 2004.

[17] H. Koser and J. H. Lang, "Magnetic induction micro machine—Part I: Design and analysis," *J. Microelectromech. Syst.*, vol. 15, no. 2, pp. 415–426, Apr. 2006.

[18] F. Cros, H. Koser, M. G. Allen, and J. H. Lang, "Magnetic induction micro machine—Part II: Fabrication and testing," *J. Microelectromech. Syst.*, vol. 15, no. 2, pp. 427–439, Apr. 2006.

[19] H. Koser, F. Cros, M. G. Allen, and J. H. Lang, "Magnetic induction micro machine—Part III: Eddy currents and nonlinear effects," *J. Microelectromech. Syst.*, vol. 15, no. 2, pp. 440–456, Apr. 2006.

[20] D. P. Arnold, "Magnetic Machines for Microengine Power Generation," Ph.D. dissertation, Georgia Institute of Technology, Atlanta, GA, Dec. 2004.

[21] A. E. Fitzgerald, C. Kingsley, and S. D. Umans Jr., *Electric Machinery*, 6th ed. New York: McGraw Hill, 2002.

[22] J. Lammeraner and M. Stafl, *Eddy Current*. London, U.K.: Iliffe, 1966, ch. 1–2.

[23] S. Das, "Magnetic Machines and Power Electronics for Power-MEMS Applications," Ph.D. Dissertation, Massachusetts Institute of Technology, Cambridge, MA, Aug. 2005.

[24] R. M. Bozorth, *Ferromagnetism*. New York, NY: IEEE Press, 1993, pp. 162–169. Reissue.

[25] D. P. Arnold *et al.*, "Electroplated metal microstructures embedded in fusion-bonded silicon: Conductors and magnetic materials," *J. Microelectromech. Syst.*, vol. 13, no. 5, pp. 791–798, Oct. 2004.

[26] ——, "Vertically laminated magnetic cores by electroplating Ni-Fe into micromachined Si," *IEEE Trans. Magn.*, vol. 40, no. 4, pp. 3060–3062, Jul. 2004.

[27] H. H. Woodson and J. R. Melcher, *Electromechanical Dynamics, Part I:, Discrete Systems*. New York: Wiley, 1968, ch. 4.

David P. Arnold (S'97–M'04) received dual B.S. degrees in electrical and computer engineering in 1999, followed by the M.S. degree in electrical engineering in 2001, from the University of Florida, Gainesville. He received the Ph.D. degree in electrical engineering at the Georgia Institute of Technology, Atlanta, in 2004.

During his graduate studies, he held research fellowships from the National Science Foundation and the Tau Beta Pi engineering honor society. In 2005, he joined the Department of Electrical and Computer Engineering at the University of Florida, Gainesville, as an Assistant Professor. His research focuses on the design, fabrication, and characterization of magnetic and electromechanical microsensors/microactuators, as well as miniaturized power and energy systems.

Dr. Arnold is also a member of Eta Kappa Nu and Tau Beta Pi.

Sauparna Das (M'03) received the B.S. degrees in electrical engineering and mathematics and the M.Eng. degree in electrical engineering in 2002 and the Ph.D. degree in electrical engineering in 2005 from the Massachusetts Institute of Technology (MIT), Cambridge.

He did his Master's thesis at Analog Devices, Inc., under a fellowship from the MIT EECS Internship program designing high-frequency dc–dc converters for cell phone power applications (2001–2002). His doctoral thesis focused on the development of magnetic machines and power electronics for Power-MEMS applications. He is currently a design engineer at Linear Technology designing power management ICs for portable electronic devices. His interests include the modeling, design and control of electromechanical systems and power electronics.

Dr. Das is also a member of Eta Kappa Nu.

Florent Cros received the B.S. and M.S. degrees in physics and materials science from the National Institute of Applied Sciences (INSA), Toulouse, France, from 1992 to 1997. He received the Ph.D. degree in microsystems from the Ecole Doctorale de Toulouse, France, in 2002.

Later, he accepted a postdoctoral position at the Georgia Institute of Technology, Atlanta, focusing on the fabrication of a high-temperature, high-power density magnetic induction micromachine (2002–2003). Currently, he is a Research & Development Engineer at CardioMEMS, Inc., Atlanta, GA.

Iulica Zana (M'98) received the B.S. (1994) and the M.S. (1995) degrees in materials science and engineering, from the University "Politehnica" of Bucharest, Romania, in 1994 and 1995, respectively. In 2003, he received the Ph.D. degree in metallurgical and materials engineering from the University of Alabama, Tuscaloosa.

From 2003 to 2004, he held a postdoctoral appointment with Prof. M. G. Allen's group at Georgia Institute of Technology, Atlanta. He is currently a Postdoctoral Research Fellow with the Center for Materials for Information Technology, University of Alabama, Tuscaloosa. He has been working on the development and implementation of high-performance magnetic materials into new microfabricated magnetic devices. His research interests span from deposition to characterization of magnetic materials.

Mark G. Allen (M'89–SM'95) received the B.A. degree in chemistry, the B.S.E. degree in chemical engineering, and the B.S.E. degree in electrical engineering from the University of Pennsylvania, Philadelphia, and the S.M. and Ph.D. degrees from the Massachusetts Institute of Technology, Cambridge, in 1989.

He joined the faculty of the Georgia Institute of Technology, Atlanta, in 1989, where he currently holds the rank of Professor and the J. M. Pettit Professorship in Microelectronics. His research interests are in the areas of micromachining and microelectromechanical systems (MEMS); in particular, the development and application of new fabrication technologies for micromachined devices and systems. He was General Co-Chair of the 1996 IEEE MEMS conference and is North American Editor of the *Journal of Micromechanics and Microengineering*.

Jeffrey H. Lang (S'78–M'79–SM'95–F'98) received the S.B., S.M., and Ph.D. degrees in electrical engineering from the Massachusetts Institute of Technology (MIT), Cambridge, in 1975, 1977, and 1980, respectively.

Currently, he is a Professor of Electrical Engineering at MIT. He has been an MIT faculty member since receiving his Ph.D. degree and his research and teaching interests focus on the analysis, design and control of electromechanical systems with an emphasis on rotating machinery, microsensors and actuators, and flexible structures. He has written over 160 papers and holds 10 patents in the areas of electromechanics, power electronics, and applied control.

Dr. Lang has been awarded four Best Paper prizes from various IEEE societies. He is a former Hertz Foundation Fellow and a former Associate Editor of *Sensors and Actuators*.